Preprint Title Control of Magnetic Anisotropy in Strained $La_{2/3}Sr_{1/3}MnO_3$ Films by a $BaTiO_3$ Overlayer in an Artificial Multiferroic System

Authors John E. Ordoñez, Lorena Marin, Luis A. Rodriguez, Pedro A. Algarabel, Jose A. Pardo, Roger Guzmán, Luis Morellón, César Magén, Etienne Snoeck, Maria E. Gomez and Manuel R. Ibarra

Publication Date 25 Okt 2019

Article Type Full Research Paper

Supporting Information File 1 Supporting_Information_Paper_JE_Ordoñez.doc; 5.4 MB

ORCID® iDs John E. Ordoñez - https://orcid.org/0000-0002-0611-4338; Pedro A. Algarabel - https://orcid.org/0000-0002-4698-3378; Jose A. Pardo - https://orcid.org/0000-0002-0111-8284; Roger Guzmán - https://orcid.org/0000-0002-5580-0043; Luis Morellón - https://orcid.org/0000-0003-3724-508X; Manuel R. Ibarra - https://orcid.org/0000-0003-0681-8260

Control of Magnetic Anisotropy in Strained $La_{2/3}Sr_{1/3}MnO_3$ Films by a $BaTiO_3$ Overlayer in an Artificial Multiferroic System

John E. Ordoñez[1*], Lorena Marín[1,2,3], Luis A. Rodriguez[1,4,5], Pedro A. Algarabel[2,6], José A. Pardo[3,6,7], Roger Guzmán[4], Luis Morellón[2,3,6], César Magén[2,4,6], Etienne Snoeck[5], María E. Gómez[1,8] and Manuel R. Ibarra[2,4,6].

[1] Department of Physics, Universidad del Valle, A.A. 25360, Cali, Colombia.

[2] Departamento de Física de la Materia Condensada, Universidad de Zaragoza, 50009 Zaragoza, Spain.

[3] Instituto de Nanociencia de Aragón (INA), Universidad de Zaragoza, 50018 Zaragoza, Spain.

[4] Laboratorio de Microscopías Avanzadas (LMA)-Instituto de Nanociencia de Aragón (INA), Universidad de Zaragoza, 50018 Zaragoza, Spain.

[5] CEMES-CNRS, 29 rue Jeanne Marvig, B.P. 94347, F-31055 Toulouse Cedex, France.

[6] Instituto de Ciencia de Materiales de Aragón (ICMA), CSIC-Universidad de Zaragoza, 50009 Zaragoza, Spain.

[7] Departamento de Ciencia y Tecnología de Materiales y Fluidos, Universidad de Zaragoza, 50018 Zaragoza, Spain.

[8] CENM, Universidad del Valle, Calle 13 No 100-00, Cali, Colombia

Email: John Edward Ordoñez – john.ordonez@correounivalle.edu.co

Abstract

We studied in detail the in-plane magnetic properties in heterostructures based on a ferroelectric $BaTiO_3$ overlayer deposited on a ferromagnetic $La_{2/3}Sr_{1/3}MnO_3$ film grown on pseudocubic (001)-oriented $SrTiO_3$, $(LaAlO_3)_{0.3}(Sr_2TaAlO_6)_{0.7}$ and $LaAlO_3$ substrates. In this configuration, the combination of both functional perovskites constitutes an artificial multiferroic system with potential applications in spintronic devices based on the magnetoelectric effect. We have grown the $La_{2/3}Sr_{1/3}MnO_3$ single layers and $BaTiO_3/La_{2/3}Sr_{1/3}MnO_3$ bilayers by pulsed-laser deposition technique. We analyzed the films structurally through X-ray reciprocal space maps, and high-angle annular dark field microscopy; magnetically, via thermal demagnetization curves and in-plane magnetization versus applied magnetic field loops, at room temperature. Our results indicate that the $BaTiO_3$ layer induces an additional strain in the $La_{2/3}Sr_{1/3}MnO_3$ layers close to their common interface. We observed that the presence of $BaTiO_3$ on the surface of tensile-strained $La_{2/3}Sr_{1/3}MnO_3$ films transforms the in-plane biaxial magnetic anisotropy present in the single layer towards an in-plane uniaxial magnetic anisotropy. Our experimental evidence suggests that this change in the magnetic anisotropy only occurs in tensile-strained $La_{2/3}Sr_{1/3}MnO_3$ film and is favored by an additional strain on the $La_{2/3}Sr_{1/3}MnO_3$ layer promoted by $BaTiO_3$ film. These findings reveal an additional mechanism that alters the magnetic behavior of the ferromagnetic layer and, consequently, deserves future in-depth research to determine how it can modify the magnetoelectric coupling of this hybrid multiferroic system.

Keywords

Interface-induced strain, magnetic anisotropy, artificial multiferroic system, $BaTiO_3$, $La_{2/3}Sr_{1/3}MnO_3$.

Introduction

In recent years, enormous interest has been shown in the multiferroic properties of the multilayered system based on $La_{2/3}Sr_{1/3}MnO_3$ (LSMO) and $BaTiO_3$ (BTO) films [1]–[5]. Each perovskite material has a particular ferroic order at room temperature, *i.e.*, ferromagnetic (FM) for LSMO and ferroelectric (FE) for BTO, and BTO/LSMO heterostructures have exhibited magnetoelectric coupling (MEC) [6]–[8]. They constitute a type of artificial hybrid multiferroic material that can be employed to build the next-generation sensors, multiple-state memory elements, magnetic read/write hard disks, actuators, etc., [9], [10]. In multilayered films, both electrical and magnetic properties of these ferroic perovskites are strongly affected by crystal lattice distortions originated by lattice-mismatched strain at film/substrate interface [11]–[14]. For the LSMO and other manganites, the effect of the substrate-induced strain on its magnetic properties in single-layer configuration has been widely studied, particularly the influence of strain on the magnetic anisotropy [15], [16]. Depending on the type and magnitude of the imposed biaxial strain (compressive or tensile) [17], the pure cubic-symmetry (or biaxial) magnetic anisotropy of the unstrained LSMO film can be altered in different ways: (i) giving rise to the appearance of a uniaxial in-plane magnetic anisotropy contribution, which is significantly stronger than the cubic one [15], [18]–[21], (ii) inducing an out-of-plane magnetic anisotropy in compressive-strained films [22]–[26], and (iii) suppressing the FM ordering in a small region of the layer, close to the substrate interface, due to large crystal deformations, resulting in

the formation of a *dead layer* with antiferromagnetic-insulating behavior [12], [27]–[31]. Moreover, it was found that a uniaxial magnetic anisotropy is artificially induced in LSMO films grown on ferroelectric BFO substrate when the polarization of the FE domains is switched into highly aligned stripe domains, inducing a magnetic easy axis in the FM layer parallel to the polarization direction [32], [33]. In all cases referred above, the magnetic anisotropy of the LSMO has been affected either by a non-FE or FE substrate on which it is deposited. However, it remains an open question about how the presence of a FE-BTO layer grown on top of an FM-LSMO film can alter its magnetic properties. This is a key point that needs to be evaluated to improve our understanding of the mechanisms driving MEC in BTO/LSMO heterostructures.

In this work, we show how the presence of a BTO layer onto an LSMO film under different substrate-induced epitaxial strains can affect the magnetic anisotropy of the LSMO layer, at room temperature. To strain the sample, we epitaxially grew BTO/LSMO bilayers on $SrTiO_3$ (STO), $(LaAlO_3)_{0.3}(Sr_2TaAlO6)_{0.7}$ (LSAT) and $LaAlO_3$ (LAO) single-crystal substrates where we choose for all of them the pseudocubic (001) direction perpendicular the substrate surface. We have grown the samples by pulsed-laser deposition and systematically varied the layers thickness. We structurally analyzed samples by reciprocal space maps (RSMs) around the pseudocubic (103) reflection in an X-ray diffractometer, and high-angle annular dark field in scanning transmission electron microscopy (HAADF-STEM). Local strain maps were reconstructed by geometric phase analysis (GPA) method on HAADF-STEM images. We magnetically analyzed samples by performing room-temperature polar plots of the remnant field, where we applied magnetic field on the plane of the sample along different directions.

Results and Discussion

Scheme 1 displays RSMs, taken around the pseudocubic (103) reflection, for the BTO (140 nm)/LSMO (27 nm) bilayers grown on (001)-oriented LAO (a), LSAT (b), and STO (c) substrates. The maps exhibit three main irregular spots corresponding to the pseudocubic (103) reflection of each material present in the heterostructures: BTO, LSMO, and substrate. We plotted the out-of-plane component of the scattering vector, Q_z (growth direction), versus its in-plane component, Q_x (associated to the [100] direction). In all cases, we noted that for the LSMO reflections the position of Q_x coincides, within the measurement margin of error, with those of the substrates, while the position of Q_z is quite different from that of each substrate, being almost superimposed for LSMO grown on LSAT (see Scheme 1 (b)). This behavior corroborates the expected fully-strained epitaxial growth (cube-on-cube) of the LSMO film where its in-plane lattice parameter is adapted to that of the substrate, and its out-of-plane lattice parameter is deformed accordingly [34], [35]. The LSMO reflection for the sample grown on LAO substrate, Scheme 1(a), exhibits a low intensity and broad spot, which is influenced by the twinned nature of the rhombohedral LAO substrate, evidenced by the splitting of the LAO main reflection into three spots.

For the BTO layers, its Q_x position is the same, within the experimental error, for all samples, and it does not coincide with the LSMO and substrate reflections, indicating that the in-plane lattice parameter of the BTO is not adapted to the substrate or to the LSMO film. Similarly, the Q_z position of the BTO reflection is also the same in all maps. Interestingly, we observed a clear splitting of the BTO reflection spot for the bilayers grown on STO and LAO substrates, indicating the possible two different out-of-plane lattice parameters. Result that we will discuss latter.

From Q_x and Q_z scattering vector components of each reflection spot, we have calculated the in-plane and out-of-plane lattice parameters of the BTO and LSMO layers in the heterostructures. We summarized such results in Table 1. We also listed the lattice deformation (in percentage) due to the induced strain in the in-plane ($f_{a\text{-}system}$) and out-of-plane ($f_{c\text{-}system}$) lattice parameter of each film, defining $f_{a\text{-}system}$ and $f_{c\text{-}system}$ as:

$$f_{a-system} = \left(\frac{a_{film-system} - a_{bulk-system}}{a_{bulk-system}} \right) \times 100 \quad (1)$$

$$f_{c-system} = \left(\frac{c_{film-system} - c_{bulk-system}}{c_{bulk-system}} \right) \times 100 \quad (2)$$

where a and c correspond to the in-plane and out-of-plane lattice parameter of the *system* and the subscript *film* and *bulk* are associated to the lattice parameters measured in the film and that reported for the bulk of each material, respectively. According to equation 1, positive (negative) values of $f_{a\text{-}system}$ correspond to tensile (compressive) strain. In table 1 we summarize the strain values. As expected from the LSMO and substrate mismatches, STO and LAO substrates induce a high compressive ($f_{a\text{-}LSMO}$ = -2.3%) and moderate tensile ($f_{a\text{-}LSMO}$ = +0.7%) strain, respectively. A very weak compressive strain ($f_{a\text{-}LSMO}$ = -0.2%) is observed in the LSMO film grown on LSAT. According to Poisson's effect, each tensile (compressive) in-plane strain led to shrinkage (elongation) of c_{LSMO}, where the higher the $f_{a\text{-}LSMO}$ magnitude the higher the $f_{c\text{-}LSMO}$ magnitude. For the BTO layers their in-plane lattice parameter is close to that of the bulk value, whereas the c_{BTO} reveals two values corresponding to the two spots observed in the RSMs (scheme 1).

Therefore, we have three scenarios that depend on the crystal distortion of the LSMO film:

(i) a bilayer with a compressive-strained LSMO film on LAO substrate

(ii) a bilayer with a weakly compressive-strained LSMO film on LSAT substrate and

(iii) a bilayer with a tensile-strained LSMO film on STO substrate.

Scheme 2 displays a scheme illustrating each case.

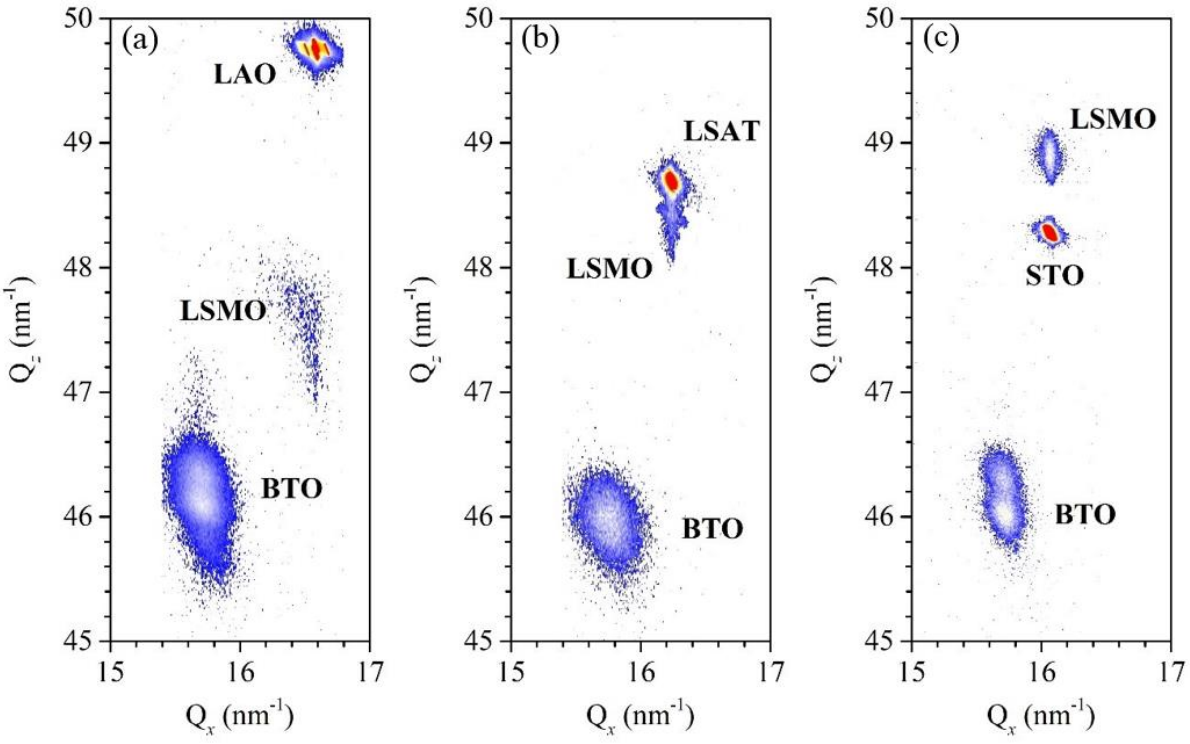

Scheme 1. X-ray reciprocal space maps around the pseudo-cubic (103) Bragg reflection for the LSMO/BTO bilayers grown on (a) LAO, (b) LSAT, and (c) STO substrates.

Table 1. In- and out-of-plane lattice parameters, *c*/*a* ratio, and lattice deformation for BTO and LSMO layers in the heterostructures (bulk values at room temperature are: $a_{LSMO} = c_{LSMO} = 3.876$ Å [36], $a_{BTO} = 3.999$ Å, $c_{BTO} = 4.033$ Å [37]).

Substrate	Film	In-plane [Å]	Out-of-plane [Å]	c/a ratio	f_a [%]	f_c [%]
LAO	*LSMO*	3.80(1)	3.98(4)	1.05(1)	-2.3(3)	+2(1)
	BTO (spot 1)	4.00(3)	4.07(1)	1.01(1)	+0.0(1)	+0.9(2)
	BTO (spot 2)	4.00(3)	4.09(1)	1.02(1)	+0.0(1)	+1.4(2)
LSAT	*LSMO*	3.869(5)	3.896(9)	1.007(4)	-0.2(1)	+0.5(2)
	BTO	4.00(3)	4.10(2)	1.03(1)	+0.0(1)	+1.7(5)
STO	*LSMO*	3.905(7)	3.855(9)	0.987(4)	+0.7(2)	-0.5(2)
	BTO (spot 1)	4.01(2)	4.07(1)	1.015(8)	+0.3(2)	+0.9(2)
	BTO (spot 2)	4.01(2)	4.09(1)	1.020(8)	+0.3(2)	+1.4(2)

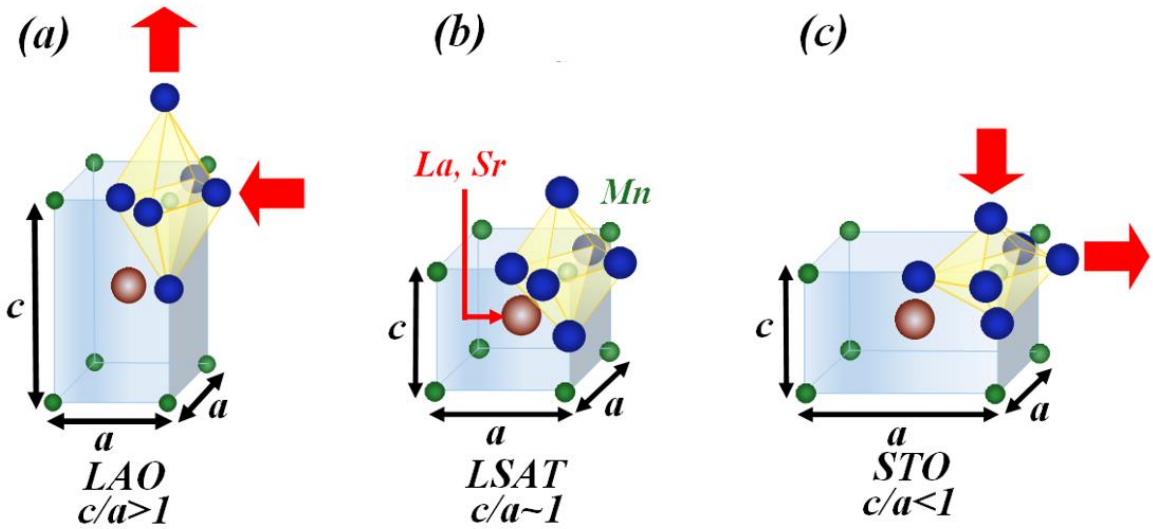

Scheme 2. Sketch of lattice distortion of the LSMO crystal cell induced by the substrate: (a) compressive-strain deformation on LAO, (b) nearly unstrained growth on LSAT, and (c) tensile-strained deformation on STO.

Scheme 3 displays isothermal room temperature loops of the normalized magnetization ($M(H)/M_s$) as a function of the applied magnetic field for 27-nm thick LSMO films (plots on the left), and for BTO(140 nm)/LSMO(27 nm) bilayers (plots on the right) grown on STO (plots on the top), LSAT (plots on the middle), and LAO (plots on the bottom) substrates. Hysteresis loops were measured by applying the magnetic field in the plane of the film along the three high-symmetry axes: [100] (black squares), [110] (blue circle), and [010] (red triangles) directions. We observe that the magnetization loop shape depend on both substrate and the applied field direction. For the LSMO film grown on STO, there is almost no difference among the three narrow hysteresis loops (Scheme 3a). For the LSMO film grown on LSAT, a narrow and nearly square-shaped loop is observed along the [110] direction (blue circles) while distorted loops due to a reduced remnant magnetization are found along the [100] (black squares) and [010] (red triangles) directions (Scheme 3c). For the film grown on LAO, broad loops with progressive reversal magnetization are observed in the three directions (Scheme 3e). For all LSMO single layers, a maximum value of M_r is found in the hysteresis loops taken along the [110] direction (blue circles), revealing that such direction constitutes an either magnetization easy axis, for a given in-plane anisotropy, or a magnetization intermediate axis for an out-of-plane anisotropy. For BTO / LSMO samples grown on LSAT (Scheme 3d) and LAO (Scheme 3f) we do not detect appreciable changes in the shape of the hysteresis loops in comparison with those for LSMO film. However, in the bilayer grown on STO (Scheme 3b), the M_r for the hysteresis loop taken along the [100] (black squares) is reduced when compared with the loop measured along the [010] direction (red triangles).

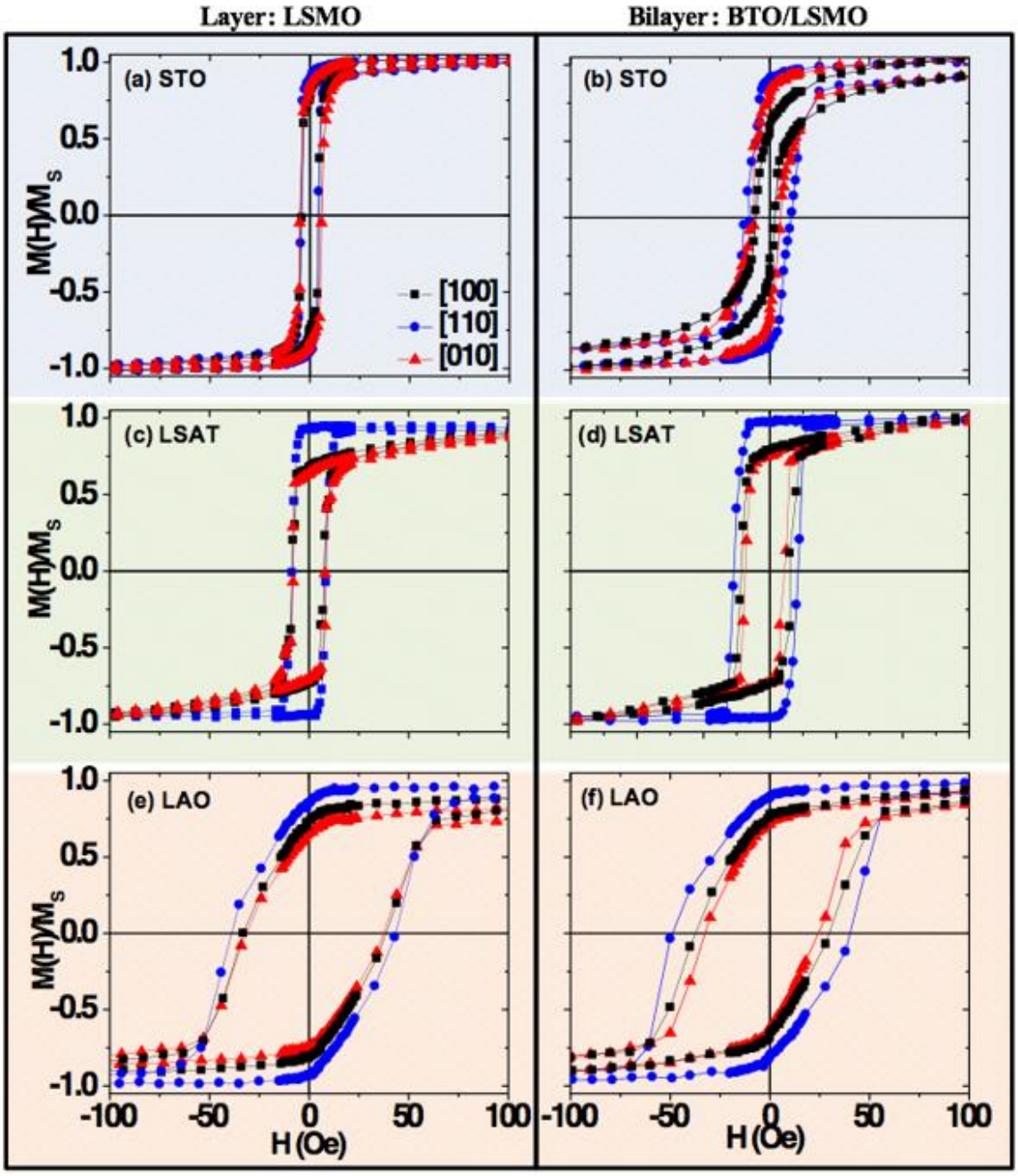

Scheme 3. Normalized isothermal hysteresis loops at 300 K for LSMO films grown on (a) STO, (c) LSAT and (e) LAO substrates, and for BTO/LSMO bilayers grown on (b) STO, (d) LSAT and (f) LAO substrates with applied field along [100] (black squares), [010] (red triangles), and [110] (blue circle) in-plane directions.

Scheme 4 displays polar magnetization plots of M_r/M_S as a function of the in-plane applied magnetic field at 300 K for a LSMO layer and for BTO/ LSMO bilayers grown on different substrates and LSMO thicknesses. Scheme 4.a shows polar plots for a

27-nm LSMO layer (black squares) and BTO (140 nm)/LSMO(27 nm) on STO; Scheme 4.b BTO(140 nm)/LSMO(27 nm) bilayers grown on STO (green triangles), LAO (purple diamonds), and LSAT (blue pentagons); Scheme 4.c. BTO(140 nm)/ LSMO(t_{LSMO}) bilayer grown on STO with t_{LSMO} = 20 nm (blue circles), 27 nm (green triangles) and 40 nm (filled black squares). For LSMO single layers (Scheme 4(a)), we observe a four-fold shape suggesting a predominant cubic-symmetry anisotropy with magnetization easy axes along four in-plane diagonal directions ([110], [$\underline{1}$10], [1$\underline{1}$0] and [$\underline{11}$0]). This type of biaxial anisotropy has been observed in unstrained and tensile-strained LSMO films [2], [15], [38]–[40]. A similar four-fold shape we also observed in the bilayers (Scheme 4 (b)) grown on LSAT and LAO, indicating that the biaxial anisotropy is preserved after the deposition of the BTO layer.

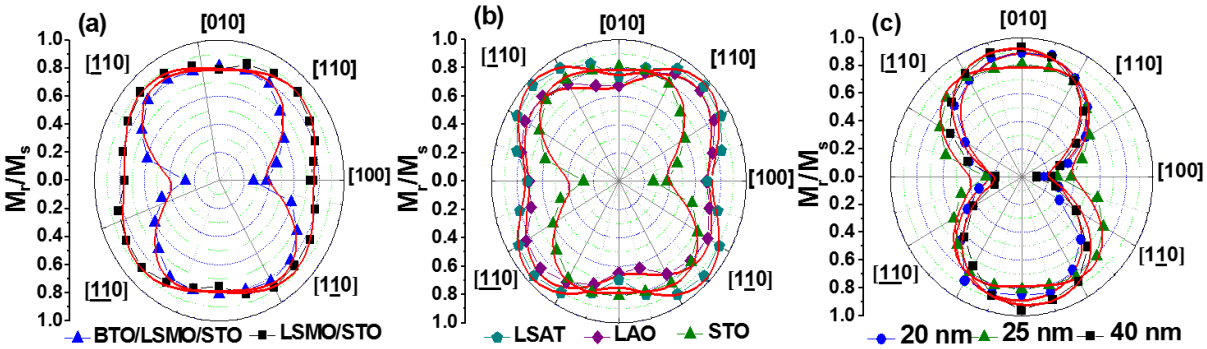

Scheme 4. Polar plots of the normalized remnant magnetization, at 300 K, for (a) LSMO(27 nm) layer (black squares) and BTO/LSMO bilayer (green triangles) grown on STO; (b) BTO/LSMO bilayers grown on STO (green triangles), LAO (purple diamonds), and LSAT (blue pentagons) substrates; (c) BTO/ LSMO) bilayer with t_{LSMO} = 20 nm (blue circles), 27 nm (green triangles) and 40 nm (black down triangles). Continuous red lines correspond to numerical fit.

Interestingly, plots show how the four-fold shape in the LSMO film grown on STO (Scheme 4-(a)) is transformed to a two-fold shape in the bilayer, with easy axis along the [010] and [0-10] directions. Such unexpected change could reflect that a 140-nm-thick BTO layer grown onto a 27-nm-thick tensile-strained LSMO film distorts its biaxial magnetic anisotropy. Moreover, a similar measurement in bilayers where we varied the thickness of the LSMO film from 20 to 40 nm, keeping constant the 140-nm thickness of the BTO layer, Scheme 4(c), proved that a predominant uniaxial anisotropy is still present in LSMO films up to 40 nm thickness.

Following a similar approach presented in Ref [19], where the total anisotropy energy of strained LSMO films contains both biaxial and uniaxial contributions, we estimated the uniaxial (k_u) and biaxial (k_1) anisotropy constants for the LSMO layer and BTO/LSMO bilayer grown on STO substrate. For the LSMO single layers, as the four-fold shape of the polar plots suggests, an important biaxial contribution exists with an average value of 4 kJ/m^3 and a negligible uniaxial contribution, with a value of k_u <0.4 kJ/m^3. For the BTO/LSMO bilayer grown on STO substrate, the presence of the BTO overlayer dramatically decreases the biaxial contribution, and both k_1 and k_u reach a similar average value of 0.4 kJ/m^3. In addition, the uniaxial contribution in the BTO/LSMO bilayer grown on STO substrate increases slightly from 0.38 $\pm$ 0.05 kJ/m^3 (for t_{LSMO} = 20 nm) to 0.55 $\pm$ 0.05 kJ/m^3 (for t_{LSMO} = 40 nm). Thus, we our experimental results permit us to conclude that the deposition of BTO in the top layer of the tensile-strained LSMO drastically changes the magnetic anisotropy of the ferromagnetic layer.

In previous studies, an emergent uniaxial contribution in LSMO films grown on (001)-oriented STO is associated to crystal distortions of the film where the tetragonal crystal structure of the tensile-strained film can be locally altered with the formation of

an orthorhombic structure due to different rotation patterns of the MnO_6 octahedra to favor epitaxial growth [39], [41]. To observe if the large mismatch between the tensile-strained LSMO and BTO systems (~ 2.35%) achieves deforming the LSMO atomic layers close to their interface, we performed a local strain study.

Scheme 5 (a) displays a HAADF-STEM image for a BTO/LSMO bilayer grown on STO substrate, where we can identify both BTO/LSMO and LSMO/STO interfaces. The insets correspond to high-magnification HAADF-STEM images to highlight the flat atomic sharp interfaces. By mean the geometric phase analysis (GPA) method at the HAADF images, it is possible to display the in-plane deformation maps (ε_{xx}), Scheme 5(b), and out-of-plane deformation maps (ε_{zz}), Scheme 5(c). The GPA strain maps are reconstructed considering a certain crystalline region as reference (in this case, the STO lattice) so they provide information about the relative difference (or relative strain) of the lattice parameters (in percentage) between a certain crystal phase and the lattice reference [42]. Such relative differences are calculated as ε_{xx} = [100 × ($a_{film\text{-}system}$ - a_{STO})/a_{STO}] and ε_{zz} = [100 × ($c_{film\text{-}system}$ - c_{STO})/c_{STO}], where a_{STO} and c_{STO} correspond to the in-plane and out-of-plane lattice parameters of the STO substrate. We can then relate the in-plane lattice deformation $f_{a\text{-}system}$ and in-plane deformation maps ε_{xx}, as well as the out-of-plane strain $f_{c\text{-}system}$ and out-of-plane deformation maps ε_{zz}, by means of the following equations:

$$f_{a-system} = \frac{a_{STO}\left(\varepsilon_{xx} + 100\right)}{a_{bulk-system}} - 100 \qquad (3)$$

$$f_{c-system} = \frac{c_{STO}\left(\varepsilon_{zz} + 100\right)}{c_{bulk-system}} - 100 \,. \qquad (4)$$

The local color variations observed in the strain maps reflect homogeneous, dislocation-free STO and LSMO layers, and a BTO layer with several linear defects. Most are concentrated close to the BTO/LSMO interfaces and are promoted by the large mismatch between the lattice parameters of the BTO and the strained LSMO film. They correspond to misfit dislocations created parallel and perpendicular to the interface and favor the relaxation of the BTO atomic layers placed far from the BTO/LSMO interface.

For a quantitative strain analysis, profiles of ε_{xx} and ε_{zz} extracted for the GPA maps are plotted in Scheme 5(d) and 5(e). These profiles are traced perpendicular to the interfaces, along two particular zones:

- *Profile 1* (blue line), the profile passes through a horizontal misfit dislocation (the misfit direction is associated to Burgers' vector direction) placed close to the interface and,
- *Profile 2* (black line), the profile is free from horizontal misfit dislocation.

For comparison between the strain results obtained by GPA and by RSMs, we plotted in-plane strain ($f_{a\text{-}system}$), Scheme 5(d), and out-of-plane strain ($f_{c\text{-}system}$), Scheme 5(e), profiles.

In *Profile 1*, we see that ε_{xx} is equal to zero, on average, inside the STO and LSMO systems to then present a discontinuity around the BTO dislocation and finally follow an increasing tendency, reaching a value of ε_{xx} = 1.54% at 37-nm thickness of BTO, and a maximum value of ε_{xx} = 2.27% at the BTO surface (see strain profile in the Supplementary Information, traced along the whole BTO thickness). A zero value of ε_{xx} between STO and LSMO is caused by adapting $a_{film\text{-}LSMO}$ with a_{STO}, while the increasing behavior of ε_{xx} observed above the dislocation is associated with the tendency of BTO to recover its unstrained in-plane lattice parameter in bulk. In terms

of f_a, we see how the substrate-induced strain elongates the in-plane lattice parameter of LSMO around 0.7%, which agrees with that calculated from RSMs. In addition, the in-plane lattice parameter of the BTO layer is compressed down to -2%, at the interface, to then relax progressively, reaching a value of f_a = -1% at 47 nm to the LSMO/BTO interface and f_a = 0% at 140 nm, just in the free BTO surface (not shown here).

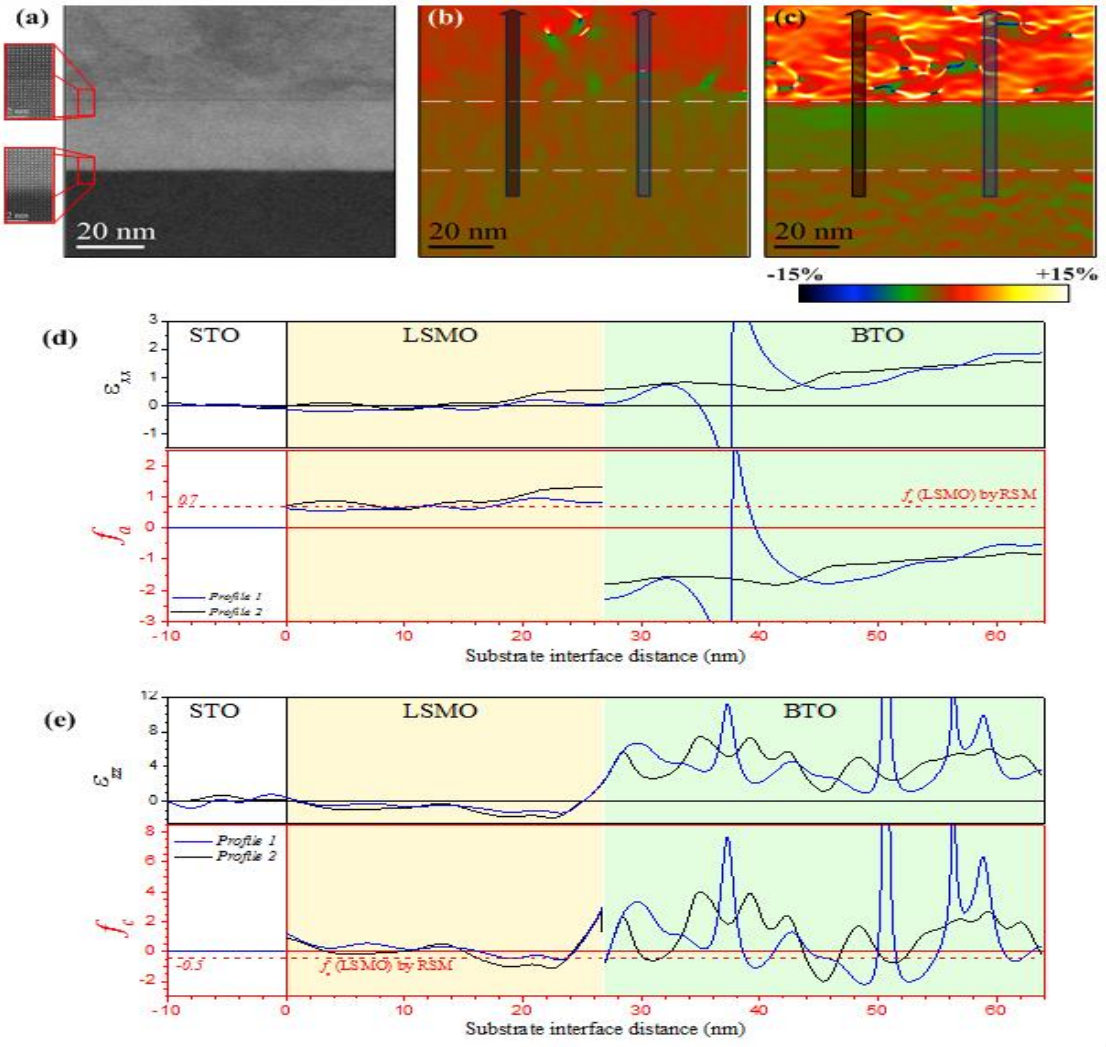

Scheme 5. (a) HAADF-STEM micrograph for a BTO/LSMO bilayer grown on STO. Insets correspond to high-magnification STEM images recorded close to the BTO/LSMO and LSMO/STO interfaces, up and down respectively. Strain maps for the in-plane ε_{xx} (b) and out-of-plane ε_{zz} (c) lattice parameters. Dotted white lines mark the interfaces. In-plane strain e_{xx} and lattice deformation, f_a, profiles (d) and out-of-

plane strain, ε_{zz}, and lattice deformation, f_c, (e) profiles. *Profile 1* (black line) passes through a region free from dislocations; *profile 2* (blue line) passes through a misfit dislocation of the BTO.

A different behavior is observed in *Profile 2*, particularly in the LSMO layer where ε_{xx} seems to not change in the first 16 nm approximately (with an average value of ε_{xx} = 0.0% and f_a = 0.7%) to then progressively increase until ε_{xx} = 0.57% (or f_a = 1.32%). This fact evidences that the BTO layer locally induces an additional tensile deformation to $a_{film\text{-}LSMO}$, up to twice that already induced by the substrate. This extra elongation of $a_{film\text{-}LSMO}$ seems to help the relaxation of the BTO layer; hence, horizontal misfit dislocations are not formed. Similar profiles were extracted from the ε_{xx} strain maps. Compared to the ε_{xx} profiles, ε_{zz} profiles present noisier behavior inherent to the GPA method [43], with an extended and strong variation around each interface that cannot allow measuring the strain close to them (around 2 nm above and below the interface). However, valuable information can be extracted from them, especially in the LSMO layer where we see that the ε_{zz} profiles follow a decrease trend. In terms of f_c, we find that the out-of-plane lattice parameter slightly elongates, by 0.3%, close to the STO/LSMO interface, and then it compresses. In *profile 1*, $c_{film\text{-}LSMO}$ experiences compressive strain up to 0.5% (*i.e.*, f_c = -0.5%), which is in good agreement with that value measured in the RSM. In *profile 2*, the compressed effect is much higher reaching a value of f_c = -1.1%.

As discussed, shrinkage of $c_{film\text{-}LSMO}$ is a direct consequence of the tensile-induced strain effect provoked by the substrate in the film; however, a small expansion close to the substrate interface has been observed in LSMO film grown on STO (001) [35] and is caused by the suppression of octahedral rotations. Again, we find that the absence of misfit dislocations close to the LSMO/BTO interface allows inducing

additional shrinkage to the out-of-plane lattice parameter of the LSMO film. Therefore, the microscopic study of the crystal strain reveals that the BTO overlayer promotes an inhomogeneous strain distribution in the LSMO atomic layers close to the BTO/LSMO interface, where the absence of BTO misfit dislocations induces additional tensile-strain effect in the surrounding LSMO lattice. Such additional strain achieves producing *c/a* ratios down to 0.976 that can be much higher just in the boundary of the LSMO/BTO interface. As demonstrated in a previous work [41], a drastic reduction of $c_{film\text{-}LSMO}/a_{film\text{-}LSMO}$ ratio favors rotation of the MnO_6 octahedra out of the plane, which results in the emergence of uniaxial anisotropy that increases with the increase of the tilting angle of the MnO_6. Thus, the uniaxial contribution of the magnetic anisotropy in the tensile-strain LSMO films comes from these extra tensile-strained regions.

Conclusion

In summary, our study on the magnetic anisotropy of an artificial ferroelectric BTO/LSMO system allows observing an unexpected in-plane uniaxial magnetic anisotropy in the ferromagnetic layer. In more detail, we found that a BTO overlayer modifies the biaxial anisotropy of tensile-strained LSMO films, grown on (001)-oriented STO substrates, towards a uniaxial anisotropy. Such change is not observed in compressive-strained LSMO films grown on (001)-oriented LSAT and LAO substrates. A microscopy analysis of the crystal deformation allows determining that the BTO overlayer locally causes a non-uniform strain distribution in the LSMO atomic layers close to the BTO/LSMO interfaces, where in some regions it provokes an additional tensile strain that, in consequence, promotes the emergence of a uniaxial anisotropy. From a magnetic point of view, this finding shows a new route to

alter the magnetic behavior of the LSMO layer, while from an applicative point +of view, it becomes a new parameter to consider in future studies to fully understand the magnetic-electric coupling effect in this particular hybrid multiferroic system.

Experimental

We grew epitaxial LSMO single layers and BTO/LSMO bilayers by the pulsed-laser deposition (PLD) technique, employing a KrF excimer laser at 248 nm pulse wavelength and 20 ns pulse duration. The films were grown on 5 × 5 × 0.5 mm^3 (001)-oriented STO, LSAT, and LAO single-layer substrates. The deposition of single LSMO films was performed at a substrate temperature of 830 °C and oxygen pressure of 400 mTorr, as described elsewhere [12], [44], followed by a cooling cycle between 830 and 20 °C at an oxygen pressure of 700 Torr to favor optimal oxygen stoichiometry, at a cooling rate of 10 °C/min. In the case of the bilayers, the BTO film was then deposited at 830 °C and an oxygen pressure of 3 mTorr. After BTO growth, samples were cooled down at an oxygen pressure of 700 Torr. We chose the thicknesses of the LSMO (t_{LSMO}) and BTO (t_{BTO}) layers at 27 and 140 nm, respectively. Only in the case of the LSMO/BTO bilayers grown on STO, a particular batch of samples was prepared with the thickness of the LSMO layer systematically varied with t_{LSMO} = 20, 27, and 40 nm, maintaining the thickness of the BTO layer constant at t_{BTO} = 140 nm.

The thickness of each individual layer was determined by X-ray reflectivity (not shown). Crystal structure analysis of each film was performed by means of reciprocal space maps (RSM) around the pseudocubic (103) reflection that permit measuring the in-plane (*a*) and out-of-plane (*c*) lattice parameter for each layer. Both measurements were performed in a Bruker D8 ADVANCE diffractometer using a

high-resolution configuration where a four-crystal Ge (220) monochromator selects the K_{a1} radiation from a Cu anode, providing an X-ray beam with a wavelength of λ = 1.54056 Å.

Local analysis of the crystalline structure of the bilayers was carried out by high-angle annular dark field scanning transmission electron microscopy (HAADF-STEM) in a probe-corrected FEI Titan Low Base 60-300 microscope operated at 300 kV with a spatial resolution below 1 Å. Local strain field maps of the bilayers were obtained by applying the geometric phase analysis (GPA) method on HAADF-STEM images.

We studied the in-plane magnetic anisotropy through room-temperature hysteresis loops taken at different angles between the in-plane applied magnetic field and the crystallographic directions by means of a vibrating sample magnetometer (VSM). For all samples, we subtracted the linear diamagnetic contribution from the STO substrate to plot the hysteresis loops. The direction variation of the external in-plane magnetic field was changed by physically rotating the sample, using a 15° step angle. From hysteresis loops, we extracted the remnant magnetization (M_r) normalized to saturation magnetization (M_S) and display them in a polar plot. The magnetic anisotropy dependence on the substrate for both, the single LSMO layer and BTO/LSMO bilayer was studied, as well as its dependence on the thickness of the LSMO layer in the bilayer film.

Acknowledgements

This work has been supported financially by the “Instituto de Nanociencia de Aragón”, Zaragoza, Spain, where the films were partially grown and characterized; Center of Excellence for Novel Materials (CENM); COLCIENCIAS-UNIVALLE research project 110656933104, contract No.2013-0002; UNIVALLE research projects CI 7978 and CI 71109. This work was also supported by the Spanish Ministry of Science (through Project MAT2014-51982-C2-R, including FEDER funding) and the Aragón Regional government (Project No. E26)."

References

1. T. X. Li, M. Zhang, F. J. Yu, Z. Hu, K. S. Li, D. B. Yu, and H. Yan, “Effect of misfit strain on multiferroic and magnetoelectric properties of epitaxial $La_{0.7}Sr_{0.3}MnO_3/BaTiO_3$ bilayer,” J. Phys. D Appl. Phys., 2012, voL 45, no. 85002, pp. 1-6.

2. H. Boschker, M. Huijben, A. Vailionis, J. Verbeeck, S. Van Aert, M. Luysberg, S. Bals, G. Van Tendeloo, E. P. Houwman, G. Koster, D. H. A. Blank, and G. Rijnders, “Optimized fabrication of high-quality $La_{0.67}Sr_{0.33}MnO_3$ thin films considering all essential characteristics,” J. Phys. D Appl. Phys., 2011, vol. 44, no. 205001, pp. 1–9.

3. S. R. Singamaneni, W. Fan, J. T. Prater, and J. Narayan, “Magnetic properties of $BaTiO_3/La_{0.7}Sr_{0.3}MnO_3$ thin films integrated on Si (100),” J. Appl. Phys., 2014, vol. 116, no. 224104, pp. 1–6.

4. J. E. Ordoñez, M. E. Gómez, W. Lopera, and P. Prieto, “Ferroelectric/ferromagnetic bilayers based on oxide materials by pulsed-laser deposition,” IEEE Trans. Magn., 2013, vol. 49, no. 8, pp. 4586–4589.

5. J. E. Ordoñez, M. E. Gómez, and W. Lopera, “Influence of ferroelectric layer on artificial multiferroic LSMO / BTO bilayers deposited by DC and RF sputtering,” Rev. Mex. Física, 2016, vol. 62, pp. 543–548.

6. W. Eerenstein, N. D. Mathur, and J. F. Scott, “Multiferroic and magnetoelectric materials,” Nature, 2006, vol. 442, no. 17, pp. 759–765.

7. W. Eerenstein, M. Wiora, J. L. Prieto, J. F. Scott, and N. D. Mathur, “Giant sharp and persistent converse magnetoelectric effects in multiferroic epitaxial heterostructures,” Nat. Mater., 2007, vol. 6, pp. 6–9.

8. T. X. Li and K. Li, “The effect of interface oxygen content on magnetoelectric effect of epitaxial $La_{0.7}Sr_{0.3}MnO_3/BaTiO_3$ bilayer,” J. Appl. Phys., 2014, vol. 116, pp. 7–11.

9. H. Béa, H. M. Gajek, M. Bibes, and A. Barthélémy, “Spintronics with multiferroics,” J. Phys. Condens. Matter, 2008, vol. 20, no. 434221, pp. 1–11.

10. S. Keshri and S. S. Rajput, “Effect of BTO addition on the structural and magnetoresistive properties of LSMO,” Phase Transitions A Multinatl. J., 2014, vol. 87, no. 2, pp. 136–147.

11. J. P. Velev, S. S. Jaswal, and E. Y. Tsymbal, “Multiferroic and magnetoelectric materials and interfaces,” Phil. Trans. R. Soc. A, 2011, vol. 369, pp. 3069–3097.

12. L. Marín, L. A. Rodríguez, C. Magén, E. Snoeck, R. Arras, I. Lucas, L. Morellón, P. A. Algarabel, J. M. De Teresa, and M. R. Ibarra, “Observation of the strain induced magnetic phase segregation in manganite thin films,” Nano Lett., 2015, vol. 15, no. 1, pp. 492–497.

13. R. K. Zheng, Y. Wang, Y. K. Liu, G. Y. Gao, L. F. Fei, Y. Jiang, H. L. W. Chan, X. M. Li, H. S. Luo, and X. G. Li, “Epitaxial growth and interface strain coupling effects in manganite film / piezoelectric-crystal multiferroic heterostructures Au PMN-PT PMN-PT,” Mater. Chem. Phys., 2012, vol. 133, pp. 42–46.

14. I. Vrejoiu, M. Ziese, A. Setzer, P. D. Esquinazi, B. I. Birajdar, A. Lotnyk, M. Alexe, and D. Hesse, “Interfacial strain effects in epitaxial multiferroic heterostructures of $PbZr_xTi_{1-x}O_3/La_{0.7}Sr_{0.3}MnO_3$ grown by pulsed-laser deposition,” Appl. Phys. Lett., 2008, vol. 92, no. 152506, pp. 20–22.

15. P. Perna, C. Rodrigo, E. Jime, F. J. Teran, N. Mikuszeit, L. Me, J. Camarero, and R. Miranda, “Tailoring magnetic anisotropy in epitaxial half metallic $La_{0.7}Sr_{0.3}MnO_3$ thin films,” J. Appl. Phys., 2011, vol. 110, no. 13919, pp. 1–10.

16. H. Boschker, M. Mathews, E. P. Houwman, H. Nishikawa, A. Vailionis, G. Koster, and G. Rijnders, “Strong uniaxial in-plane magnetic anisotropy of (001)- and (011)-oriented $La_{0.67}Sr_{0.33}MnO_3$ thin films on $NdGaO_3$ substrates,” Phys. Rev. B 79(21), 2009, No. 214425.

17. Y. Suzuki, H. Y. Hwang, S. Cheong, T. Siegrist, and R. B. Van Dover, “Magnetic anisotropy of doped manganite thin films and crystals,” J. Appl. Phys., 2013, vol. 83, no. 7064, pp. 1–4.

18. M. Mathews, F. M. Postma, J. C. Lodder, R. Jansen, G. Rijnders, G. Rijnders, and D. H. A. Blank, “Step-induced uniaxial magnetic anisotropy of $La_{0.67}Sr_{0.33}MnO_3$ thin films,” Appl. Phys. Lett., 2005, vol. 87, no. 242507, pp. 1–3.

19. H. Boschker, M. Mathews, P. Brinks, E. Houwman, A. Vailionis, G. Koster, D. H. A. Blank, and G. Rijnders, “Uniaxial contribution to the magnetic anisotropy of $La_{0.67}Sr_{0.33}MnO_3$ thin films induced by orthorhombic crystal structure,” J. Magn. Magn. Mater., 2011, vol. 323, no. 21, pp. 2632–2638.

20. P. Perna, C. Rodrigo, E. Jiménez, N. Mikuszeit, F. J. Teran, L. Méchin, J. Camarero, and R. Miranda, “Substrate-induced magnetic anisotropy in $La_{0.7}Sr_{0.3}MnO_3$ epitaxial thin films grown onto (110) and (118) SrTiO3 substrates,” J. Phys. Conf. Ser., 2011, vol. 303, no. 12058, pp. 1–6.

21. M. Ziese, “Magnetocrystalline anisotropy transition in $La_{0.7}Sr_{0.3}MnO_3$ films,” p hys. stat. sol., 2005, vol. 13, pp. 116–117.

22. H. Boschker, J. Kautz, E. P. Houwman, G. Koster, and D. H. A. Blank, “Magnetic anisotropy and magnetization reversal of $La_{0.67}Sr_{0.33}MnO_3$ thin films on $SrTiO_3$(110),” J. Appl. Phys., 2010, vol. 108, no. 103906, pp. 1–6.

23. C. Kwon, M. C. Robson, K.-C. Kim, J. Y. Gu, S. E. Lofland, S. M. Bhagat, Z. Trajanovic, M. Rajeswari, T. Venkatesan, A. R. Kratz, R. D. Gomez, and R. Ramesh, “Stress-induced effects in epitaxial $(La_{0.7}Sr_{0.3})MnO_3$ films,” J. Magn. Magn. Mater., 1997, vol. 172, pp. 229–236.

24. L. Ranno, A. Llobet, and R. Tiron, “Strain-induced magnetic anisotropy in epitaxial manganite films,” Appl. Surf. Sci., 2002, vol. 188, pp. 170–175.

25. Y. Wu, Y. Suzuki, U. Rüdiger, J. Yu, and A. D. Kent, “Magnetotransport and magnetic domain structure in compressively strained colossal magnetoresistance films,” Appl. Phys. Lett., 1999, vol. 75, pp. 19–22.

26. R. Desfeux, S. Bailleul, A. Da Costa, and W. Prellier, “Substrate effect on the magnetic microstructure of $La_{0.7}Sr_{0.3}MnO_3$ thin films studied by magnetic force microscopy,” Appl. Phys. Lett., 2012, vol. 78, no. 2001, pp. 67–70.

27. J. Z. Sun, D. W. Abraham, R. A. Rao, and C. B. Eom, “Thickness-dependent magnetotransport in ultrathin manganite films Thickness-dependent magnetotransport in ultrathin manganite films,” Appl. Phys. Lett., 1999, vol. 74, pp. 3017–3019.

28. R. P. Borges, W. Guichard, J. G. Lunney, J. M. D. Coey, F. Ott, R. P. Borges, W. Guichard, J. G. Lunney, and J. M. D. Coey, “Magnetic and electric ‘dead’ layers in ($La_{0.7}Sr_{0.3}$) MnO_3 thin films,” J. Appl. Phys., 2001, vol. 89, no. 7, pp. 3868–3873.

29. M. Angeloni, G. Balestrino, N. G. Boggio, P. G. Medaglia, P. Orgiani, and A. Tebano, “Suppression of the metal-insulator transition temperature in thin $La_{0.7}Sr_{0.3}MnO_3$ films,” J. Appl. Phys., 2004, vol. 96, no. 11, pp. 6387–6392.

30. C. Aruta, G. Ghiringhelli, V. Bisogni, L. Braicovich, N. B. Brookes, A. Tebano, and G. Balestrino, “Orbital occupation, atomic moments, and magnetic ordering at interfaces of manganite thin films,” Phys. Rev. B, 2009, vol. 80, pp. 1–8.

31. J. Fontcuberta, D. Pesquera, G. Herranz, A. Barla, E. Pellegrin, F. Bondino, E. Magnano, and F. Sa, “Surface symmetry-breaking and strain effects on orbital occupancy in transition metal perovskite epitaxial films,” Nat. Commun., 2012, vol. 3, no. 1189, pp. 1–7.

32. L. You, B. Wang, X. Zou, Z. S. Lim, Y. Zhou, H. Ding, L. Chen, and J. Wang, “Origin of the uniaxial magnetic anisotropy in $La_{0.7}Sr_{0.3}MnO_3$ on stripe-domain $BiFeO_3$,” Phys. Rev. B, 2013, vol. 88, no. 184426, pp. 1–9.

33. J. T. Heron, D. G. Schlom, R. Ramesh, J. T. Heron, D. G. Schlom, and R. Ramesh, “Electric field control of magnetism using BiFeO3-based heterostructures,” Appl. Phys. Rev., 2015, vol. 1, no. 12303, pp. 1–18.

34. A. Tebano, C. Aruta, P. G. Medaglia, F. Tozzi, G. Balestrino, A. A. Sidorenko, G. Allodi, R. De Renzi, G. Ghiringhelli, C. Dallera, L. Braicovich, and N. B. Brookes, “Strain-induced phase separation in $La_{0.7}Sr_{0.3}MnO_3$ thin films,” Phys. Rev. B, 2006, vol. 74, no. 245116, pp. 1–7.

35. A. Vailionis, H. Boschker, Z. Liao, J. R. A. Smit, G. Rijnders, M. Huijben, and G. Koster, “Symmetry and lattice mismatch induced strain accommodation near and away from correlated perovskite interfaces,” Appl. Phys. Lett., 2014, vol. 105, no. 131906, pp. 1–5.

36. M. C. Martin and G. Shirane, “Magnetism and structural distortion in the $La_{0.7}Sr_{0.3}MnO_3$ metallic ferromagnet,” Phys. Rev. B., 1996, vol. 53, no. 21, pp. 285–290.

37. S. Sharma, M. Tomar, A. Kumar, and N. K. Puri, “Stress induced enhanced polarization in multilayer $BiFeO_3/BaTiO_3$ structure with improved energy storage properties,” AIP Adv., 2016, vol. 107216, no. 2015, pp. 0–8.

38. M. Ziese, H. C. Semmelhack, and P. Busch, “Sign reversal of the magnetic anisotropy in $La_{0.7}A_{0.3}MnO_3$ (A = Ca , Sr , Ba , & □) films,” J. Magn. Magn. Mater., 2002, vol. 246, pp. 327–334.

39. J. M. Vila-Fungueiriño, C. T. Bui, B. Rivas-Murias, E. Winkler, J. Milano, J. Santiso, and F. Rivadulla, “Thermodynamic conditions during growth determine the magnetic anisotropy in,” J. Phys. D Appl. Phys., 2016, vol. 49, no. 315001, pp. 1–6.

40. K. Steenbeck and R. Hiergeist, “Magnetic anisotropy of ferromagnetic $La_{0.7}(Sr,Ca)_{0.3}MnO_3$ epitaxial films,” Appl. Phys. Lett., 1999, vol. 75, no. 12, pp. 1778–1780.

41. A. Rajapitamahuni, L. Zhang, M. A. Koten, V. R. Singh, J. D. Burton, E. Y. Tsymbal, J. E. Shield, and X. Hong, “Giant Enhancement of Magnetic Anisotropy in Ultrathin Manganite Films via Nanoscale 1D Periodic Depth Modulation,” Phys. Rev. Lett., 2016, vol. 116, no. 187201, pp. 1–6.

42. M. J. Hÿtch, E. Snoeck, and R. Kilaas, “Quantitative measurement of displacement and strain fields from HREM micrographs,” Ultramicroscopy, 1998, vol. 74, no. 3, pp. 131–146.

43. Y. Zhu, C. Ophus, J. Ciston, and H. Wang, “Interface lattice displacement measurement to 1 pm by geometric phase analysis on aberration-corrected HAADF STEM images,” Acta Mater., 2013, vol. 61, no. 15, pp. 5646–5663.

44. L. Marín, L. Morellón, P. A. Algarabel, L. A. Rodríguez, C. Magén, J. M. De Teresa, and M. R. Ibarra, “Enhanced magnetotransport in nanopatterned manganite nanowires,” Nano Lett., 2014, vol. 14, no. 2, pp. 423–428.